Physics and Chemistry of Radiation Driven Cloud Evolution. [C II] Kinematics of IC 59, and IC 63

Miranda Caputo[1,2] , Archana Soam[2,3] , B-G Andersson[2] , Remy Dennis[4], Ed Chambers[2] , Rolf Güsten[5] ,
Lewis B. G. Knee[6] , and Jürgen Stutzki[7]

[1] Ritter Astrophysical Research Center, University of Toledo Dept. of Physics and Astronomy, 2801 W. Bancroft Street, Toledo, OH 43606,
USA; miranda.caputo@rockets.utoledo.edu
[2] SOFIA Science Center, USRA, NASA Ames Research Center, M.S.-12, N232, Moffett Field, CA 94035, USA
[3] Indian Institute of Astrophysics, II Block, Koramangala, Bengaluru 560034, India
[4] Santa Clara University, 500 El Camino Real, Santa Clara, CA 95053, USA
[5] Max Planck Institut für Radio Astronomie, Bonn, Germany
[6] Herzberg Astronomy and Astrophysics Research Centre, National Research Council of Canada, 5071 West Saanich Road, Victoria, BC, V9E 2E7, Canada
[7] I. Physikalisches Institut der Universität zu Köln, Zülpicher Straße 77, D-50937 Köln, Germany

Abstract

We used high-resolution [C II] 158 μm mapping of two nebulae IC 59 and IC 63 from SOFIA/upGREAT in conjunction with ancillary data of the gas, dust, and polarization to probe the kinematics, structure, and magnetic properties of their photodissociation regions (PDRs). The nebulae are part of the Sh 2-185 H II region that is illuminated by the B0 IVe star γ Cas. The velocity structure of each PDR changes with distance from γ Cas, which is consistent with driving by the radiation. Based on previous far-ultraviolet (FUV) flux measurements of, and the known distance to, γ Cas, along with the predictions of 3D distances to the clouds, we estimated the FUV radiation field strength (G_0) at the clouds. Assuming negligible extinction between the star and clouds, we find their 3D distances from γ Cas. For IC 63, our results are consistent with earlier estimates of distance from Andersson et al., locating the cloud at ∼2 pc from γ Cas at an angle of 58° to the plane of the sky behind the star. For IC 59, we derive a distance of 4.5 pc at an angle of 70° in front of the star. We do not detect any significant correlation between the orientation of the magnetic field and the velocity gradients of [C II] gas, which indicates a moderate magnetic field strength. The kinetic energy in IC 63 is estimated to be an order of 10 higher than the magnetic energies. This suggests that kinetic pressure in this nebula is dominant.

1. Introduction

Radiation from newly formed, hot, high-mass O and B stars can give rise to a number of dynamical and chemical effects in the surrounding material. Ionizing radiation from these young stars can cause exposed material in the surrounding cloud to photoevaporate and ionize the inner boundaries of the expanding H II regions. Existing density enhancements on the peripheries of expanding H II regions create bright-rimmed clouds (BRCs). The bright rim produced by the recombination radiation from the ionization front (IF) on their surface faces the ionizing source.

High energy radiation from ionizing sources causes feedback processes in the surrounding medium. This feedback can be positive or negative, causing triggered star formation or quenching of star formation, respectively. A systematic investigation is required on the injection of mechanical energy and radiative heating efficiency in regions that are dominated by different processes (stellar winds, thermal expansion, and radiation pressure). However, some numerical simulations, such as Lancaster et al. (2021), shed controversy on the importance of stellar winds, leaving mainly thermal expansion and photoevaporation. The [C II] line uniquely probes the kinematics of the gas exposed to the mechanical energy input

by massive stars, and therefore directly measures the mechanical energy injection into the medium. Observations of the [C II] line suggest that that winds could dominate for early-type stars, while thermal expansion dominates for later-type stars (e.g., Pabst et al. 2020). The dominant processes in photon-dominated regions (PDRs) depends not only on the stellar spectral type but also on the evolutionary state of the system, internal pressures, and the geometry and distance of the clouds from the star. The case of IC 59 and IC 63 presents an interesting example in which the feedback from a B0 star is dominated by photevaporation. The radiative feedback processes act directly on the PDR, while mechanical feedback is transmitted through the PDR to the cloud interiors.

Associated with these H II regions and BRCs, PDRs, can be described as the regions in the interstellar medium (ISM) where UV radiation dominates the photochemistry (Hollenbach & Tielens 1997; Wolfire et al. 2022). These PDRs are found in the transitional regions between the ionized, atomic material and the colder, denser, molecular material in the clouds. UV radiation can infiltrate the denser gas in these PDR regions, exciting, ionizing, and affecting the gas motion; inducing chemical, thermal, and dynamical changes; and, possibly, triggering star formation. These features make PDRs important laboratories for probing the physics, chemistry, and evolution of the ISM.

The Sh 2-185 H II region that was created by the B0 IVe star γ Cas (Figure 1) is among the nearest of the well-defined systems of PDRs, it is located at a distance of 190 ± 20 pc, and
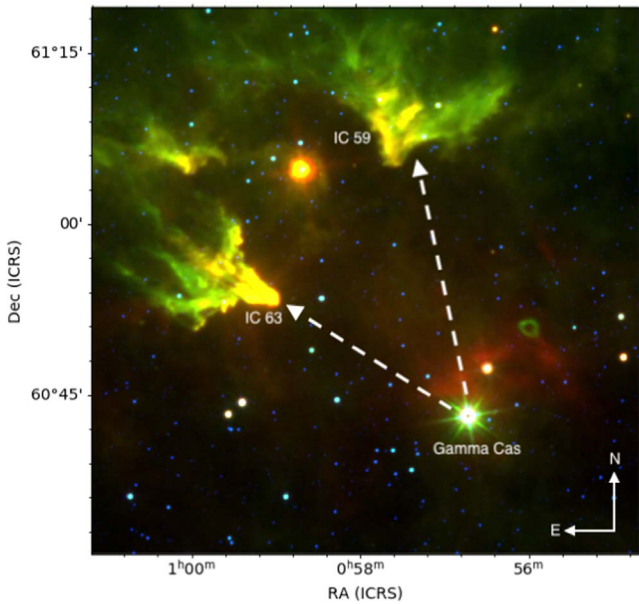
Figure 1. RGB image of the Sh 2-185 H II region made from WISE W1 (3.4 μm) in blue, W3 (12 μm) in green, and W4 (22 μm) in red.

consists of the IC 63 and IC 59 nebulae (Osterbrock 1957; France et al. 2005; Miao et al. 2010; Andersson et al. 2013; Soam et al. 2017). Because of its brightness and proximity to the Sun, Sh 2-185 is an ideal laboratory to better test the modern theoretical PDR models, and to understand their structure and kinematics.

The brighter of these clouds, IC 63, has been observed through various studies and surveys, and is composed of several clumps with varying characteristics. Jansen et al. (1994, 1995, 1996a, 1996b) performed an extensive, multi-line tracer survey of IC 63, and interpreted their relatively low spatial resolution data with comprehensive physical and chemical modeling without resolving the structure of the cloud itself. Using interferometric maps in HCO$^+$ ($J = 1$–0), Polehampton et al. (2005) showed a highly compressed ridge on the star-facing side of IC 63, which is consistent with numerical models of BRCs (Miao et al. 2009). Fleming et al. (2010) used H$_2$ (0–0)S(2) through S(5) excitation to show a temperature gradient across the cloud. Because the shape of IC 59 is not represented by most BRC models (Miao et al. 2009), Miao et al. (2010) proposed and modeled an idealized M-type BRC morphology based on IC 59 structure, and supported the conclusion from Karr et al. (2005) that there is no active star formation in IC 59.

Andrews et al. (2018) used infrared emission from both IC 63 and IC 59 to study the PAHs in these PDRs. They concluded that both IC 63 and IC 59 are experiencing photo-evaporation due to radiation from γ Cas and that the tips of each nebula are further away from γ Cas than their respective projected distances. They also used archival Herschel and Spitzer maps and line spectroscopy of IC 63 and IC 59, using spectral energy distributions to measure the far-ultraviolet (FUV) radiation field strength. They performed PDR modeling of the [C II] and [O I] lines, and the infrared continuum to derive the density and temperatures of these clouds.

Along with surveys of gas and dust tracers, another of the many ways in which these clouds have been studied is through starlight polarization observations to investigate magnetic fields. PDRs are

an ideal environment for the study of grain alignment mechanisms, in particular the radiative alignment torque (RAT) theory (Lazarian & Hoang 2007; Andersson et al. 2013; Hoang et al. 2015). Soam et al. (2017) mapped the magnetic fields in a region containing IC 63 and IC 59 using optical polarization measurements. The magnetic fields were found to be ordered. In IC 63, the field lines were found to be almost parallel to the direction of illuminating radiation and almost perpendicular in the case of IC 59. These investigations were done to understand the magnetized evolution of these nebulae. Polarization efficiency and collisional disalign-ment of dust grains in IC 63 are studied by Soam et al. (2021d) and Soam et al. (2021a), respectively. The gradients in temperature and densities in the PDR region of IC 63 are also studied by Soam et al. (2021c) using pure rotational molecular hydrogen observations.

High-sensitivity observations of a PDR line tracer at high-spectral resolution is necessary to probe the kinematics of the region. SOFIA upGREAT velocity maps of [C II] are ideal for tracing PDRs. In this paper, our focus is on understanding the kinematics, structure, and geometry of these nebulae using [C II] emission.

This paper is structured as follows. Section 2 describes the observations and data reduction. Section 3 presents the detailed analysis. The results of the gas and dust emissions and cloud kinematics, magnetic field and velocity gradients, and the FUV radiation strength estimation in IC 63 are given in Section 4. In Section 5, we discuss our findings. Section 6 summarizes our results and describes proposed further work.

2. Data Acquisition and Reduction

We observed [C II] 158 μm line emission toward IC 63 and IC 59 using the upgraded German Receiver for Astronomy at Terahertz Frequencies (upGREAT) (Heyminck et al. 2012; Risacher et al. 2016) on board the Stratospheric Observatory for Infrared Astronomy (SOFIA) (Young et al. 2012). The upGREAT Low Frequency Array (LFA) is a 14 pixel array (two 7 pixel arrays with orthogonal polarizations) that observes at $\sim$2 THz. Observations of both sources were made as part of the SOFIA project 05_0052 (PI: B-G Andersson).

The IC 63 observations were made on a $\sim$50 minutes flight leg on 2017 February 1. To create the map, we used the total power on-the-fly mode (TP OTF), scanning in the N-S direction. The map size was 288$''$ $\times$ 252$''$, as seen by the central LFA pixel. The step size between spectral readouts along each scan row was 6$''$, and the spacing between scan rows was 6$''$. The integration time in each readout was 0.7 s pixel^{-1}, which translates to $\sim$10 s of on-source integration time, given the spatial multiplexing advantage of 14 pixels.

The IC 59 observations were carried out during six flight legs in 2017, on 8, 9, 10, and 14 February, and 13 and 15 June. The total flight leg time for these six legs was $\sim$3.5 hr. The IC 59 region was covered with two different TP OTF maps. The first, larger map is 600$''$ $\times$ 540$''$, as seen by the central LFA pixel, and covers the entire nebula. The second, smaller map is 468$''$ $\times$ 294$''$, and is rotated by 25$°$ (counter-clockwise) relative to the J2000 coordinate frame. The sky position of the second map was optimized to cover the [C II] emission detected in the first map. Both IC 59 maps have 6$''$ between readouts along each scan row and 6$''$ separation between rows. The total on-source integration time per map point in the combined map is $\sim$14 s.

All of the data was calibrated by the GREAT instrument team using their *kalibrate* software (Guan et al. 2012). Main

beam efficiencies for each pixel were applied (values ranged from 0.59 to 0.68). We fit second order baselines to a narrow spectral region (-21 to $+21$ km s^{-1} for both IC 63 and IC 59) after masking out the line region (-4 to $+4$ km s^{-1} for IC 63, -5 to $+5$ km s^{-1} for IC 59). The final data cubes were gridded onto $7\farcs5$ pixels, and spectrally smoothed to 0.4 km s^{-1}. To remove spectral baselines and create the final data cube, we used the CLASS[8] software package.

We also used HCO$^+$ ($J = 1$–0) position-position–velocity maps observed with CARMA[9] (Soam et al. 2021b), and molecular hydrogen H$_2$ (1–0)S(1) mapping from CFHT[10] (Andersson et al. 2013) in conjunction with low-resolution ^{12}CO (1–0) data from TRAO[11] as part of a molecular line survey of 16 BRCs by A. Soam et al. (2023, in preparation) to help in studying the gas locations at different opacities. Visual extinction data was obtained from a Vilnius-system[12] Archival 70 and 250 -μm maps from Herschel PACS and SPIRE, WISE 22 μm maps, Spitzer IRAC 8 μm, and IPHAS[13] Hα (Drew et al. 2005; Barentsen et al. 2014) maps of the regions were used to better understand the dust properties of the clouds.

3. Analysis

3.1. Dust and Gas Emissions

Figure 2 shows two RGB images of IC 63 created with the upGREAT [C II] integrated intensity map in red, CFHT H$_2$ (1–0)S(1) map in green, CARMA HCO$^+$ ($J = 1$–0) integrated intensity map in blue in the top panel, and IPHAS Hα emission in blue in the middle panel.

Figure 3 shows RGB images of IC 59 with [C II] in red, H$_2$ (1–0)S(1) in green, TRAO ^{12}CO (1–0) integrated intensity map in blue in the upper panel and as IPHAS Hα in blue in the middle panel. The intensity levels for each color in Figures 2 and 3 were chosen to provide a balance between signal-to-noise and the desire to best represent all of the data in the images. The CFHT H$_2$ (1–0)S(1) and the IPHAS Hα images were star subtracted.[14]

The lower panels in Figures 2 and 3 illustrate the regions and naming conventions that will be used in the rest of this paper for IC 63 and IC 59, respectively.

Figure 4 shows integrated intensity maps of [C II] and HCO$^+$ ($J = 1$–0), and dust emission maps from Herschel PACS 70 and SPIRE 250 μm, WISE 22 μm, and Spitzer IRAC 8 μm for IC 63. Panel (c) is the HCO$^+$ ($J = 1$–0) integrated intensity map from panel (b) zoomed in and with the intensities stretched to show the fainter emission near the second clump that is only visible when saturating the high emission region to the west. Figure 5 shows the same maps as Figure 4 for IC 59 but without HCO$^+$ ($J = 1$–0) maps.

---

8 CLASS is part of the Grenoble Image and Line Data Analysis Software (GILDAS; Pety 2005), which is provided and actively developed by IRAM, and is available at http://www.iram.fr/IRAMFR/GILDAS.

9 The Combined Array for Research in Millimeter-wave Astronomy. https://en.wikipedia.org/wiki/Combined_Array_for_Research_in_Millimeter-wave_Astronomy.

10 Canada–France–Hawaii Telescope. https://www.cfht.hawaii.edu/.

11 Teaduk Radio Astronomical Observatory at the Korea Astronomy and Space Science Institute. https://trao.kasi.re.kr/main.php.

12 VILNIUS is a medium-band, seven-color photometeric system (UPXYZVS).

13 The International Photometric Hα Survey of the northern galactic plane. http://www.iphas.org/.

14 Images were star subtracted thanks to the program Starnet++, found at https://sourceforge.net/projects/starnet/.

Each map from Figures 4 and 5 has the corresponding beam size plotted in the lower left-hand corner and a physical scale for reference (0.01 pc for IC 63 and 0.1 pc for IC 59) on the lower right-hand corner, assuming the clouds are 200 pc away. All maps other than the [C II] integrated intensity map are over plotted with smoothed black or white contours of the corresponding [C II] integrated intensity map with levels at [10, 15, 20, 25, 30, 35, 40] K km s^{-1}, $\sim$20-80% of the maximum integrated intensity of 50 K km s^{-1} for IC 63 and [10, 13, 16, 20] K km s^{-1}, $\sim$33–66% of the maximum integrated intensity of 30 K km s^{-1} in IC 59.

3.2. Velocity Channel Maps

Figure 6 shows a velocity channel map of [C II] in IC 63 obtained from our SOFIA/upGREAT position-position–velocity data, moving from the blueshifted velocity component of ~ -2 km s^{-1} on the top left-hand to the blueshifted velocity component ~ 3.4 km s^{-1} on the bottom right-hand. Contours are at levels 4 to 20 K km s^{-1} in steps of 4 K km s^{-1}. The velocity channel map of [C II] for IC 59 is shown in Figure 7 with the same general properties as Figure 6 but with velocities from -2.5 to ~ 2.9 km s^{-1}, labels on the lower right-hand, and contours at levels 2, 5, and 8 K km s^{-1}.

3.3. Position–Velocity Diagrams

The upper panels of Figures 8 and 9 show gray-scale [C II] integrated intensity maps with numbered arrows where slices have been taken through the position-position–velocity upGREAT [C II] data cubes of IC 63 and IC 59. The position–velocity (PV) diagrams from these slices are shown in the lower panels of the figures, with velocities from ~ -3 through 4 km s^{-1} for IC 63 and ~ -4 through 3 km s^{-1} for IC 59. HCO$^+$ ($J = 1$–0) data from slice 5 in IC 63 is also shown on the bottom panel for Figure 8 from -1 to 1.5 km s^{-1} in two different color stretches to show the slight emission at an offset of $\sim 2\farcm5$. The offset begins at $0'$ from the base of each arrow from the upper panels and concludes at the tips of the arrow heads.

4. Results

4.1. Dust and Gas Relations

4.1.1. IC 63

As can be seen in Figures 2 and 4, the highest intensity regions of IC 63 are the fishhook feature inside the main clump, the small clump, and the front edge in those maps where the resolution is good enough to see it. The other noticeable, but less intense, features are the upper and lower tails that appear to stream from the different clumps. The 250 μm map from Herschel SPIRE, panel (g) in Figure 4, has a background source to the west of the PDR that is not seen in any other map shown in Figure 4. This object is not being considered in our analysis.

In low-resolution ($44''$) observations of IC 63 using CO ($J = 1$–0) from TRAO, the emission was seen in the main clump, but the small clump was not detected (A. Soam et al. 2023, private communication). The small clump is detected in HCO$^+$ ($J = 1$–0) and [C II] emissions.

The dense gasses, such as HCO$^+$ ($J = 1$–0), mainly trace the fishhook feature. Meanwhile, the ionized gas, traced by Hα, appears around the areas of the lowest optical depth, such as the
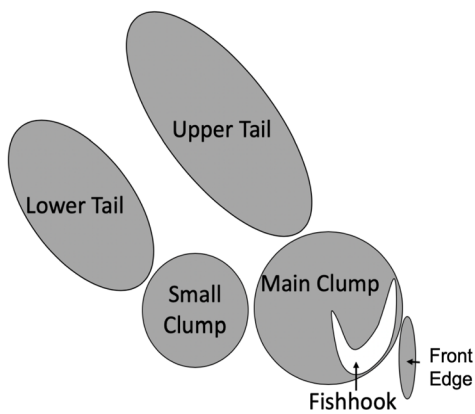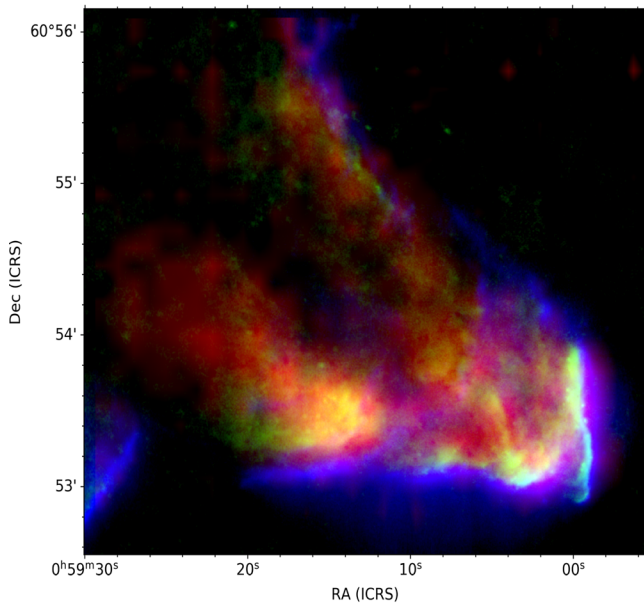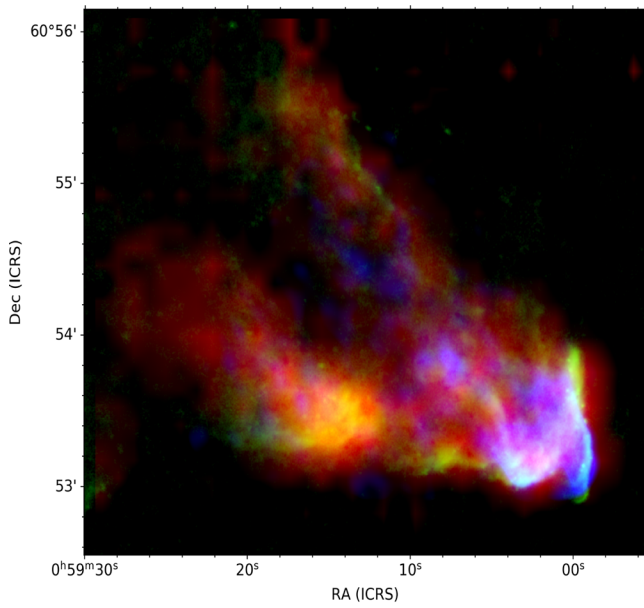
Figure 2. Top panel: Three-color, RGB image of IC 63 made with SOFIA upGREAT [C II] integrated intensity map in red, CFHT H_2 (1–0)S(1) in green, and CARMA HCO^+ ($J = 1$–0) integrated intensity in blue. Middle panel: RGB with [C II] in red and H_2 (1–0)S(1) in green like above, but blue is IPHAS $H\alpha$ emission. Lower panel: Model of IC 63 with naming conventions.
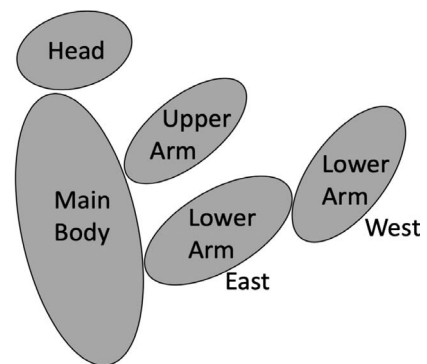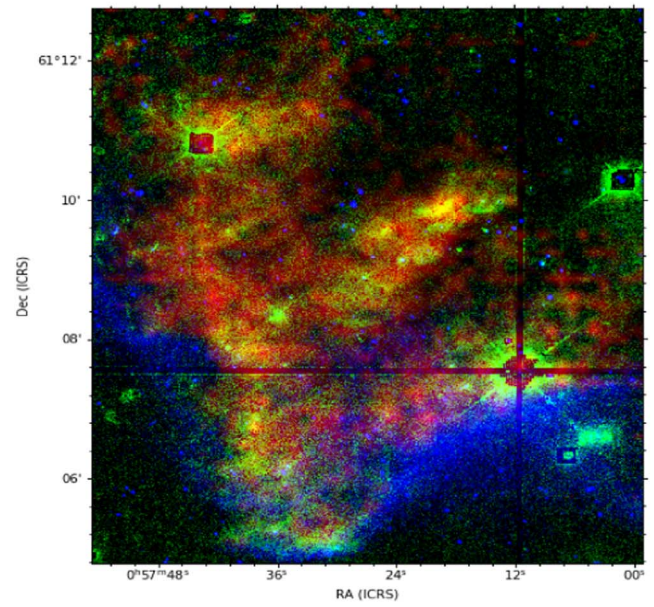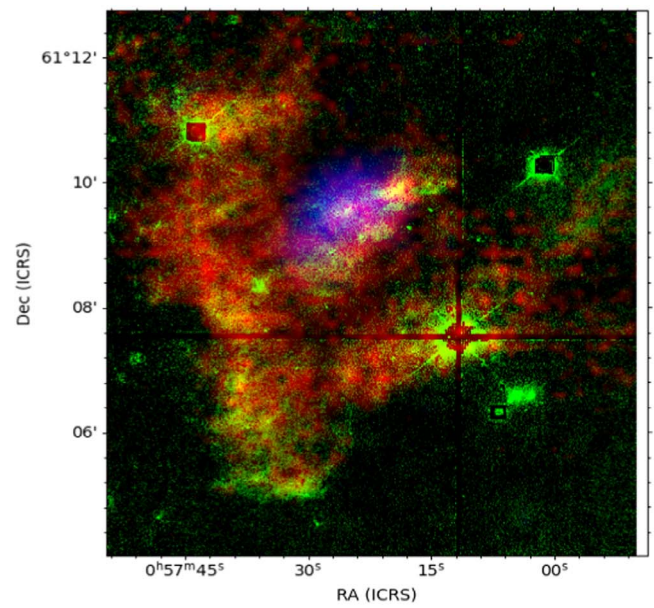
Figure 3. Same as Figure 2 but for IC 59 and the blue in the upper panel is ^{12}CO (1–0) integrated intensity. Remnants of the imperfect star subtraction and chip boundaries can be seen in the CFHT H_2 (1–0)S(1), green, emission.

western edges of the main and small clumps as well as the upper tail. $H\alpha$ is also present over the majority of the main clump at a slightly lower emission.
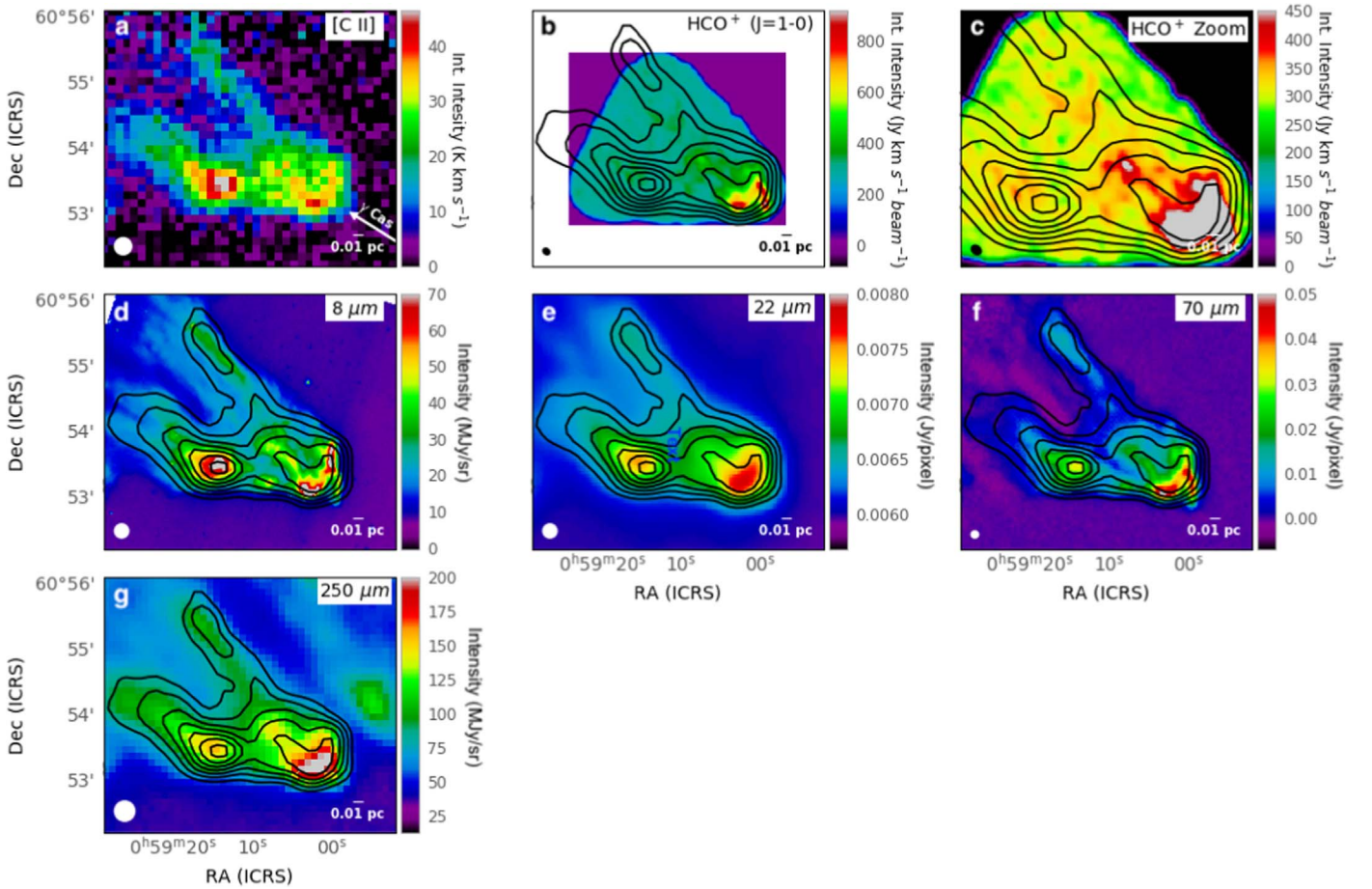
Figure 4. False color images of dust tracers and integrated intensity maps of HCO$^+$ ($J = 1-0$) and [C II]. Dust tracer maps are Spitzer IRAC 8 μm, WISE 22 μm, and Herschel PACS 70 μm and SPIRE 250 μm maps. Overlaid black contours show smoothed [C II] integrated intensity, panel (a), at levels [10, 15, 20, 25, 30, 35, 40] K km s^{-1}. Panel (c) is a zoomed in and stretched image of panel (b). All panels are labeled on the top right corner with the related map name, lower left with beam size, and lower right with a 0.01 pc scale reference except for panel (c), where this is located in the upper left. Panel (a) also has a white arrow showing the plane of the sky projection from γ Cas as reference.

The tail features lie slightly off of the radial line from γ Cas found to the southwest (see white arrow in Figure 4 panel (a)). Andersson et al. (2013) argued that, if the angle discrepancy between the projected radial vector from γ Cas and the angle of the tails is due to projection effects, then the line between the star, γ Cas, and the nebula, IC 63, makes an angle of $\sim$58° with respect to the plane of the sky.

4.1.2. IC 59

IC 59, seen in Figures 3 and 5, has multiple regions of high intensity. The brightest region is the upper arm, followed by the main body and the head. The eastern and western regions of the lower arm are the least bright regions. The TRAO observations of ^{12}CO (1–0) toward IC 59 only traces the upper arm area, while the Hα traces only the bottom ridge of the nebula without overlapping with any of the other tracers, unlike what is seen in IC 63. A slight enhancement in the H$_2$ fluorescence can be seen on the star-ward side of the CO detection, which is reminiscent of the much stronger detection in IC 63.

4.2. Cloud Velocities

4.2.1. IC 63

One of the most noticeable features of Figure 6 is the intensity shift from west to east as the velocities move from negative to positive. The most blueshifted velocity region of the nebula is the western edge of the main clump, including the fishhook and front edge, which also happens to be where Hα and H$_2$ (1–0)S(1) are dominant (see Figure 2). This region disappears in the more positive velocities, where the rest of the cloud is visible.

As can also be seen with the PV diagrams in Figure 8, the small clump, slice 4, seems to span the largest velocity ranges from $\sim$-1 km s^{-1} through 3 km s^{-1}, while the main clump/fishhook, slice 6, seems to only range from ~-2 km s^{-1} through 1 km s^{-1}. The wide range in velocities that are covered by the small clump leads to a larger integrated intensity, as seen in Figure 4 panel (a), even though the peak intensities never surpass those of the fishhook. This could mean that the small clump is less dense and cooler than the fishhook region.

Slice 5 in Figure 8 shows that the main clump region, including the fishhook and front edge, is much more blueshifted in velocity than the small clump, with average velocities of $\sim$0 and 1.5 km s^{-1}, respectively. The location of the HCO$^+$ ($J = 1-0$) emission coincides with the emission of [C II].

Slice 2 shows that the tails are somewhat blueshifted in velocity along the outer edges of the nebula, where some Hα is seen in Figure 2, while being redshifted toward the area in between the two tails.
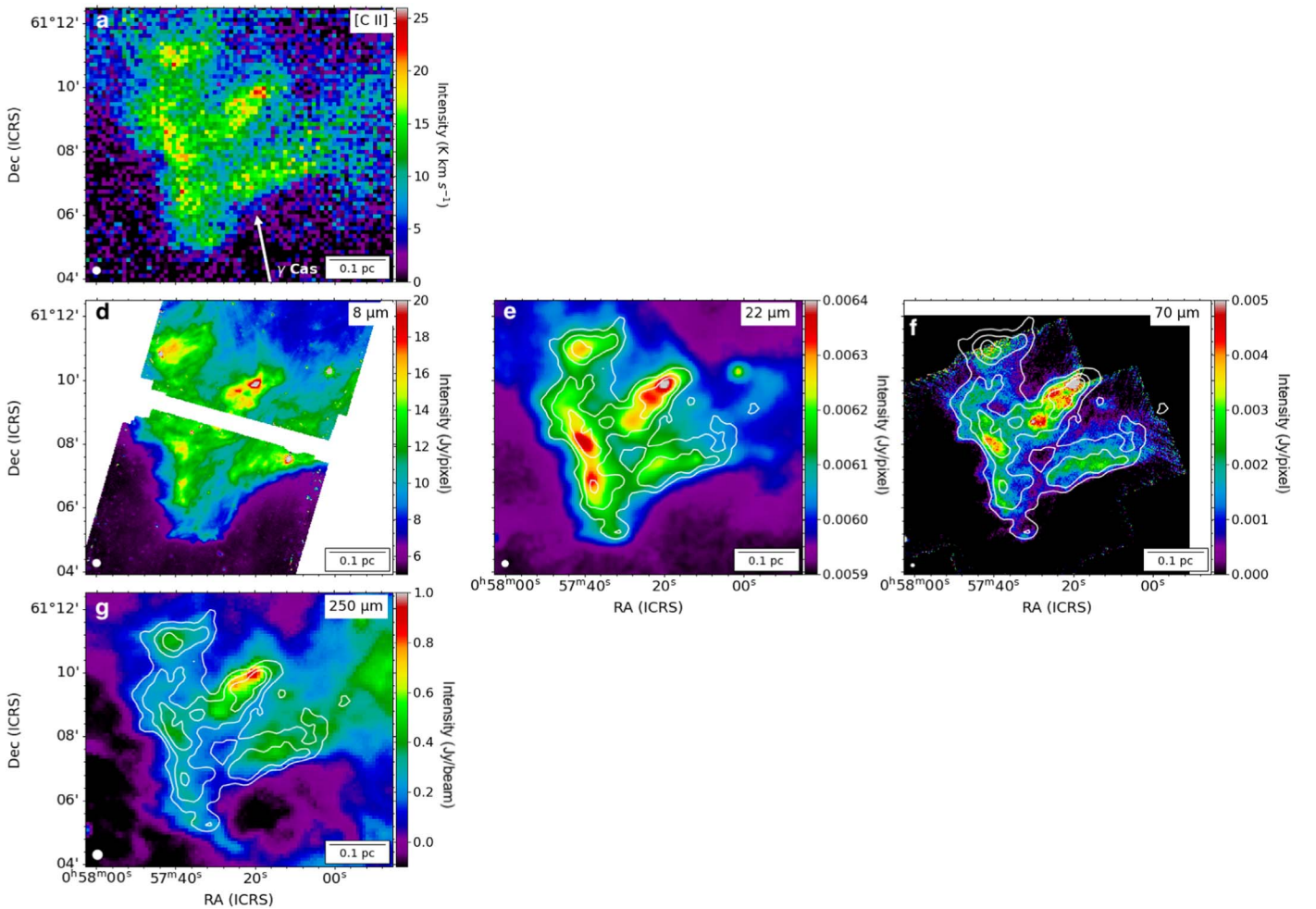
Figure 5. Same emission maps from Figure 4 but for IC 59 and without HCO$^+$ ($J = 1–0$). Overlaid black and white contours show smoothed [C II] integrated intensity, panel (a), at levels [10, 13, 16, 20] K km s^{-1}. All panels are labeled on the lower right with a 0.1 pc scale reference.

4.2.2. IC 59

The velocity channel map of [C II] in IC 59, shown in Figure 7, seems to follow similar patterns to IC 63 in Figure 6, but in opposite velocity directions. The majority of the cloud is blueshifted in velocity and is clearly visible until -0.5 km s^{-1}, where it begins to disappear. The main body, eastern lower arm, and the upper arm are the only regions that persist into the positive velocities. The highest intensity region, the upper arm, goes $\sim$1 km s^{-1} further into the positive velocities than any other region.

The upper arm of IC 59, where CO is detected and is shown in blue in the upper panel of Figure 3, is comparable to the main clump/fishhook region of IC 63 because these are the densest regions of each cloud. This is also where a faint H$_2$ fluorescent ridge can be seen. By comparing these two high density regions in each cloud, we find a contrast in their movements when compared to the rest of the clouds. The high density region in IC 63 contains, and is surrounded by, the most negative [C II] velocities seen in the cloud, while we see the opposite in IC 59 with the most positive velocities seen in and around the high density region of the upper arm.

Slice 1 of Figure 9 shows that the outside of the two arms are redshifted in velocity, while the space between them is blueshifted. In comparison, slice 2 of Figure 8 shows that IC 63 is the opposite, where the outside of the tails are

blueshifted and the area in between is redshifted. This suggests that the ionized gases toward the outside of both the arms and tails are traveling in opposite directions from our perspective.

4.3. Spectral Line Features in Different Regions of the Nebulae

The lower panels of Figures 10 and 11 show spectra that have been extracted from the SOFIA/upGREAT [C II] position-position–velocity cube regions for IC 63 and IC 59, respectively, along with the spectra for HCO$^+$ ($J = 1–0$) from these same regions in IC 63. The regions are over plotted and numbered on the gray-scale [C II] integrated intensity maps in the upper panels of each figure. Each of the spectra in the lower panels have been fitted with a single Gaussian function to derive their quantitative properties, which are listed in Tables 1 and 2 for IC 63 and IC 59, respectively.

The differences in peak $T_{\rm mb}$ between the two clouds is very obvious in these tables, with the most intense regions in IC 59 having about the same peak intensity as the two weakest regions in IC 63. The central velocities also vary, with IC 63 going from $\sim$0 to 1 km s^{-1} and IC 59 ranging from -0.5 to -1.2 km s^{-1}.

Most of the spectra for IC 63 in Figure 10 show a slight but systematic asymmetry, with a more gradual rise on the blue side and a steeper drop off on the red for [C II] and a fairly uniform shape for HCO$^+$ ($J = 1–0$).
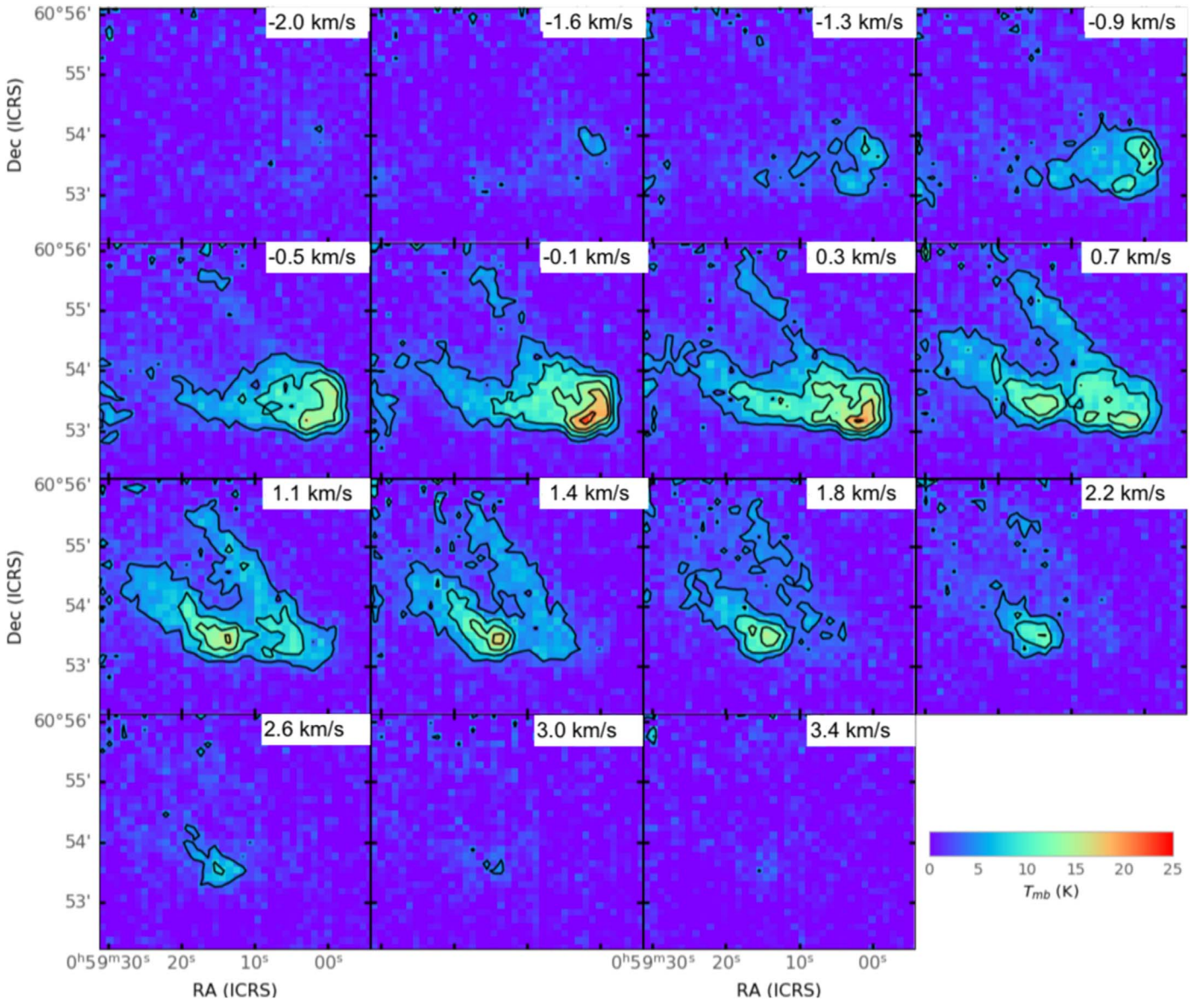
Figure 6. False color channel map of [C II] for IC 63. The corresponding velocity for all channels are marked in the upper right-hand corner of each panel.

4.4. Velocity Gradients and Magnetic Fields

To understand any relationship between gas velocity and magnetic fields, we calculated velocity gradient of [C II] emission and compared those with magnetic field orientations taken from Soam et al. (2017). These gradients are not absolute velocities but indicate local accelerations. Gradients were calculated by taking the difference between the central velocities—estimated through fitting each pixel's velocity spectrum with a Gaussian—of the pixels a specified distance from a central pixel. Only velocity gradients with less than a 20° error in angle are used. Different step distances, 2 versus 4 pixels, were used for IC 63 and IC 59, respectively, to best show the dynamics for the clouds. A larger step size was needed for the gradients in IC 59 due to the cloud being much larger than IC 63 and the pixel-to-pixel velocity change being smaller.

Figure 12 shows the local velocity gradient vectors of IC 63 and IC 59 overlaid in black on their respective central velocity maps. Previously published magnetic field orientations from

Andersson et al. (2013) and Soam et al. (2017) for both nebulae obtained from observations of partially extinguished starlight from stars located behind the nebula are plotted with white line segments. It is hard to draw any firm conclusions on the relative orientations of the velocity gradients and magnetic field lines. However, there are some hints of the magnetic fields being perpendicular to the velocity gradients in both the nebulae. High-resolution polarization observations in longer wavelengths may shed more light on this investigation.

5. Discussion

5.1. FUV Radiation Field at IC 63

The FUV radiation field (G_0) incident on IC 63 from γ Cas has been estimated by various previous studies. Jansen et al. (1995), using the projected distance between γ Cas and IC 63 of 1.3 pc and a distance to γ Cas of 230 pc, found that G_0 at IC 63 was 650 units of the Draine field (Draine 1978). Andrews et al. (2018) used dust emissions in IC 63 instead of spectral emissions from γ Cas and found a G_0 of 150, which indicates
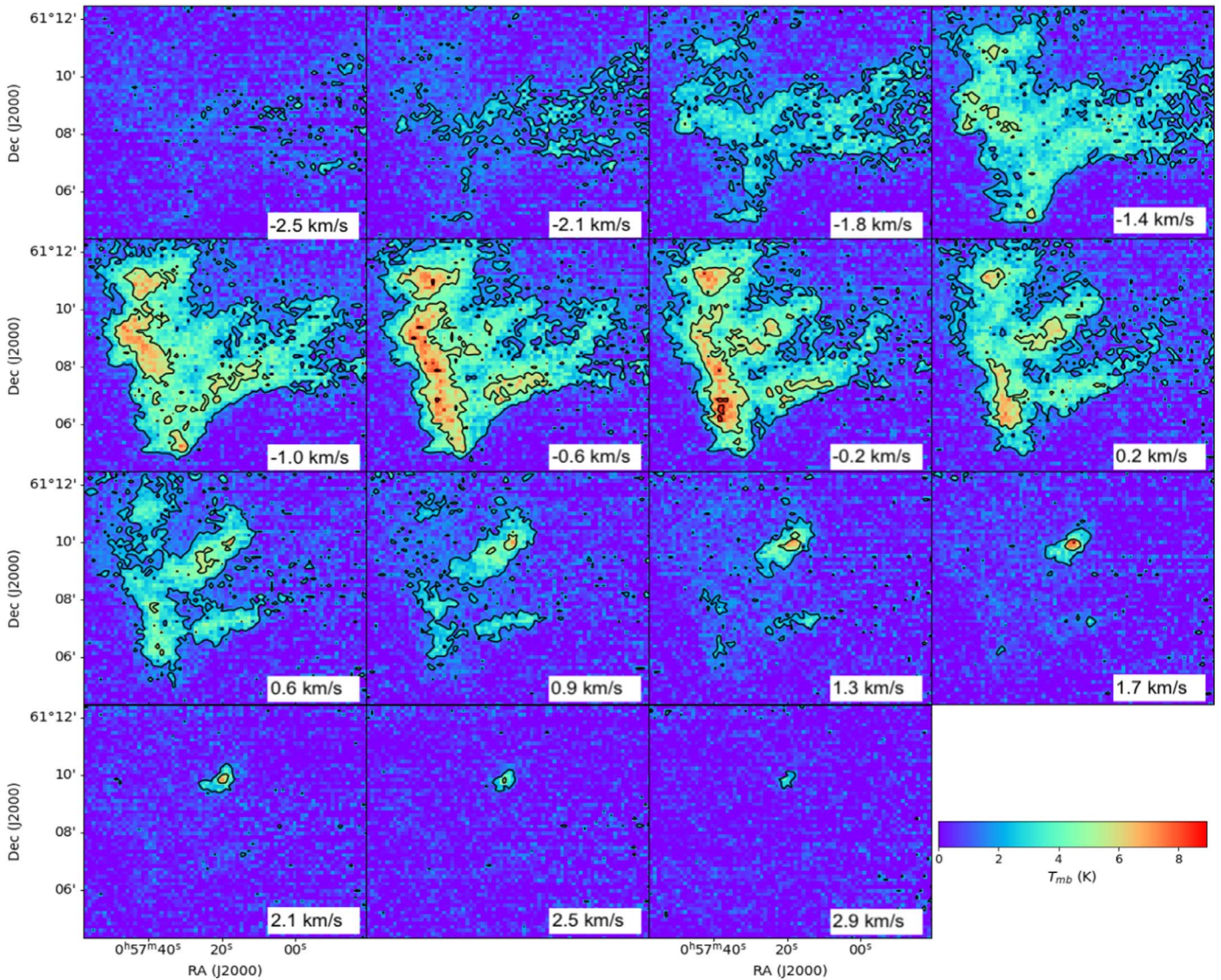
Figure 7. Same as Figure 6 but for IC 59.

that the nebula was further away than what Jansen et al. (1995) assumed as the projected distance. Andersson et al. (2013) proposed that, based on the angle of the streaming tails in IC 63, the cloud lies behind γ Cas at an angle of 58°, which makes the true distance between γ Cas and IC 63 $\sim$2 pc.

Since γ Cas is a variable star, comparing the FUV spectra from Code & Meade (1979), used by Jansen et al. (1995), to a newer spectrum from France et al. (2005), gives a better idea of what the star may have been like during the measurements of IC 63 shown by Andrews et al. (2018), as well as systematic errors in the processes used. It is found that the flux from the France et al. (2005) spectra is $\sim$.65$\times$ the flux found in the work by Code & Meade (1979). Using both of these spectra, the newer parallax to γ Cas, and a distance from γ Cas to IC 63 of 2 pc, we find that G_0 at IC 63 is 115 and 175 from France et al. (2005) and Code & Meade (1979), respectively.

5.2. FUV Radiation Field at IC 59

We are unable to estimate a G_0 for IC 59 in the same way as we did in Section 5.1 for IC 63 because IC 59 has a mostly vertical orientation in the plane of the sky, which would

mitigate any projection effects from an inclination angle. Using the projected distance from γ Cas to IC 59 of 1.5 pc provides a G_0 that is far higher than the 25 found by Andrews et al. (2018). There may be a possibility of leakage of factors FUV radiation field due to clumpiness in the clouds. To find the inclination angle for IC 59, we will assume that the G_0 from Andrews et al. (2018) and our methods used in Section 5.1 are correct because our calculated G_0 for IC 63 agrees, within statistical errors, with the 150 that Andrews et al. (2018) found.

Utilizing these assumptions, we calculate that a distance of 4.5 pc from γ Cas to IC 59 will produce a G_0 of 25. This distance corresponds to an inclination angle of 70° with respect to the plane of the sky. Figure 13 shows the proposed geometry for the IC 59–γ Cas system as viewed from the side.

5.3. Kinetic versus Magnetic Energy

In IC 63, Figure 12 upper panel, the [C II] velocity gradients show a fairly connected system that moves from velocities of almost $0 \, \text{km s}^{-1}$ at the main clump into the velocities of $1 \, \text{km s}^{-1}$ or more in the tails. No obvious structural correlation
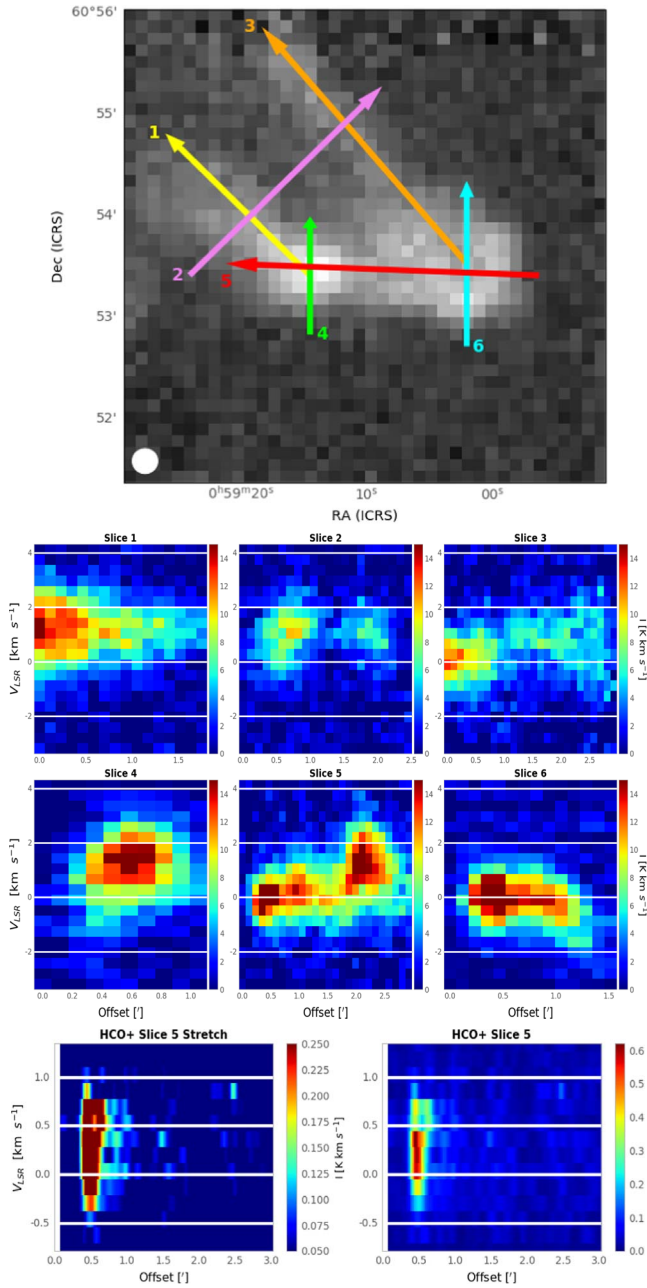
Figure 8. Upper panel: Gray-scale [C II] integrated intensity map of IC 63 with arrows indicating where and in which direction PV slices were taken. Middle panel: PV diagrams for the six slices, shown in upper plot, are plotted over the same velocity range, from -3 to 4 km s^{-1}, and represented by the same color scale. PV diagrams representing slices along the tails are on the top row while those representing the clumps are on the bottom. Lower panel: PV diagrams for slice 5 in HCO$^+$ ($J = 1$–0) and formatted as above. The image on the left-hand has had the colors stretched to see the the velocity intensity peak around an offset of $2\rlap{.}'5$. The image on the right-hand has a more even color map.

Figure 9. Same as Figure 8 but for IC 59 and with PV slices plotted from -4 to 3 km s^{-1}.

could be found when comparing the local velocity gradients and the magnetic field orientations at IC 63.

In IC 59, the data do not show a connected system (see lower panel of Figure 12). There is slightly more anticorrelation observed between the local velocity gradients and the magnetic field orientations in IC 59 than what was observed in IC 63. As described in Soam et al. (2017), this may be related to the concave shape created by UV radiation on the star-facing side. The field lines follow this concave shape of the cloud rather than going along the radiation direction as seen in IC 63
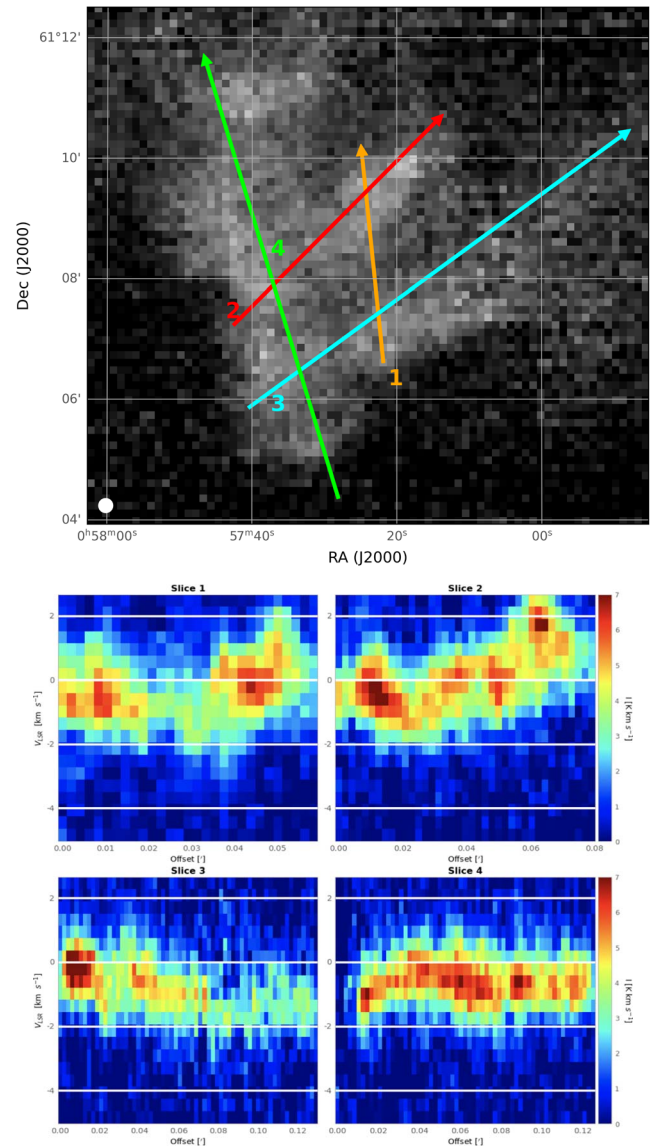
Soam et al. (2017) found the dynamical pressure in IC 63 to be less than the magnetic pressure, and both were less than the external pressure for IC 63. Using their magnetic field strength average over the main body of the PDR (region II in their Figure 1) and an average velocity change in our velocity gradients, we estimate magnetic and kinetic energy values of $E_{\mathrm{mag}} = 3.4 \times 10^{32}$ J and $E_{\mathrm{kin}} = 3.8 \times 10^{42}$ J, respectively, which suggests that the kinetic energy dominates the magnetic energy in IC 63.

5.4. Geometry of the System

Given that we have found that each nebula lies off the plane of the sky due to actual distances from the stars to the nebula being larger than the projected distances, we attempted to find whether the nebulae were in front of or behind γ Cas.

For IC 63, the RGB images in Figure 2, the shifting features seen in the channel map in Figure 6, the PV diagrams in Figure 8, and the velocity gradients in Figure 12, indicate that the blueshifted [C II] gas, where $v < 0$ km s^{-1}, is correlated with the Hα emission, which is likely due to photoevaporation. This correlation is shown

Figure 11. Same as Figure 10 but for five regions in IC 59 and with extracted spectra filled in gray. The fit parameters for each Gaussian are shown in Table 2.
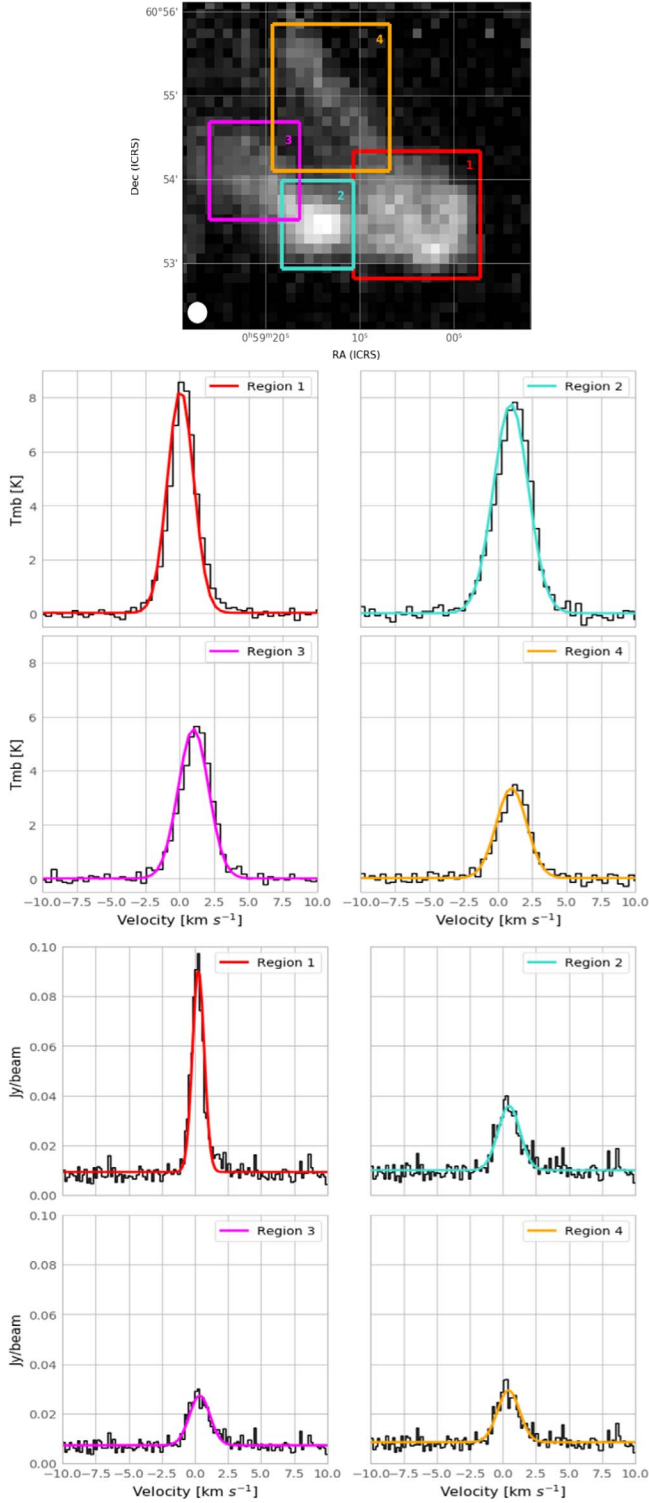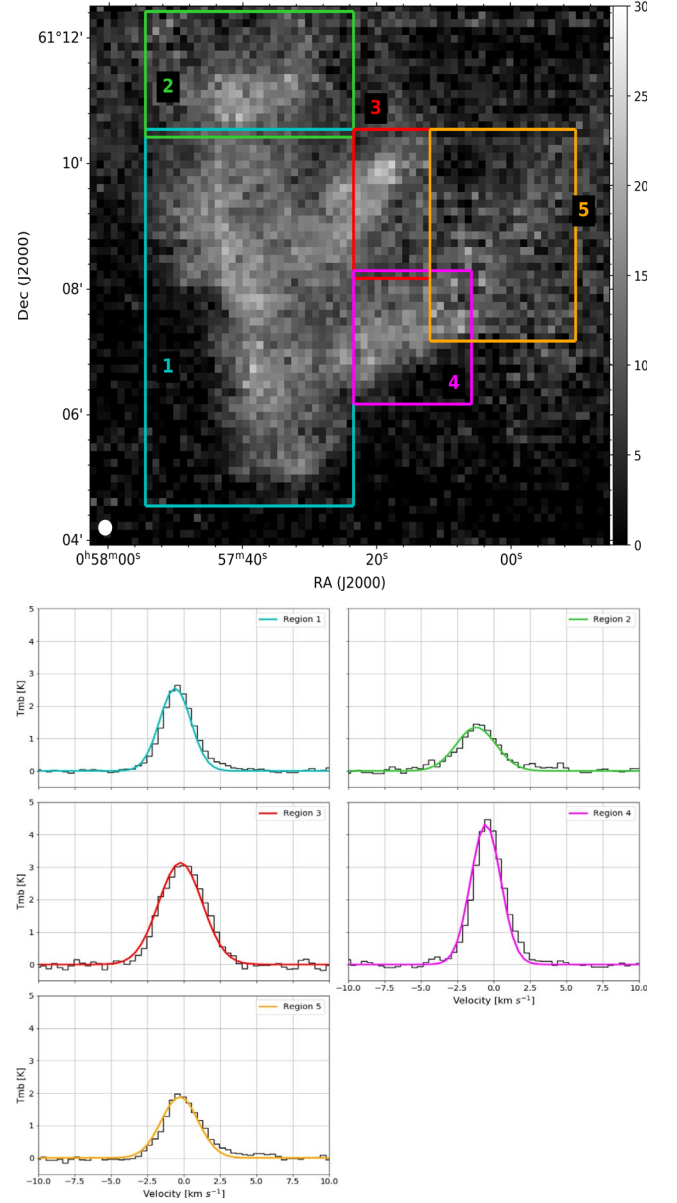

Figure 10. Upper panel: Boxed boundaries for the four main regions of IC 63 overlaid on the [C II] integrated intensity map, shown in gray-scale. Middle panel: Averaged line extraction spectra of [C II], black, from each of the four regions from above with a Gaussian fitted in the same color as the region box it represents. Lower panel: Averaged line extraction spectra from HCO$^+$ ($J = 1$–0) over the same regions and colors as [C II]. The fit parameters for each Gaussian are shown in Table 1.

in Figure 14, where the same RGB image as the middle panel of Figure 2, with red as [C II] integrated intensity, green as H$_2$ (1–0)S (1), and blue as Hα, has been plotted with Hα contours in blue and

Table 1
Table of the Parameters for the Gaussian Fitted to the [C II] and HCO$^+$ ($J = 1$–0) Velocity Spectra of IC 63 for Each Region in Figure 10

Region C II	$V_{peak} \pm \sigma_{V_{peak}}$ (km s^{-1})	FWHM $\pm \sigma_{FWHM}$ (km s^{-1})	$T_{mb} \pm \sigma_{T_{mb}}$ (K)
1	0.06 ± 0.01	2.2 ± 0.03	8.28 ± 0.10
2	0.95 ± 0.02	3.0 ± 0.05	7.77 ± 0.11
3	1.0 ± 0.02	2.6 ± 0.06	5.55 ± 0.10
4	1.0 ± 0.03	2.6 ± 0.08	3.36 ± 0.09

Region HCO$^+$	$V_{peak} \pm \sigma_{V_{peak}}$ (km s^{-1})	FWHM $\pm \sigma_{FWHM}$ (km s^{-1})	$I_{peak} \pm \sigma_{I_{peak}}$ (Jy beam^{-1})
1	0.27 ± 0.01	1.04 ± 0.03	0.082 ± 0.002
2	0.47 ± 0.05	1.96 ± 0.11	0.026 ± 0.001
3	0.37 ± 0.04	1.81 ± 0.10	0.020 ± 0.001
4	0.43 ± 0.05	1.96 ± 0.12	0.021 ± 0.001

Table 2
Table of the Parameters for the Gaussians Fitted to the [C II] Velocity Spectra
of IC 59 for Each Region in Figure 11

Region C II	$V_{peak} \pm \sigma_{V_{peak}}$ (km s^{-1})	FWHM $\pm \sigma_{FWHM}$ (km s^{-1})	T_{mb} (K)
1	-0.58 ± 0.01	2.5 ± 0.03	2.6 ± 0.03
2	-1.2 ± 0.05	3.2 ± 0.11	1.3 ± 0.04
3	-0.21 ± 0.02	3.5 ± 0.05	3.1 ± 0.04
4	-0.53 ± 0.01	2.4 ± 0.03	4.3 ± 0.05
5	-0.26 ± 0.03	3.0 ± 0.06	1.9 ± 0.04
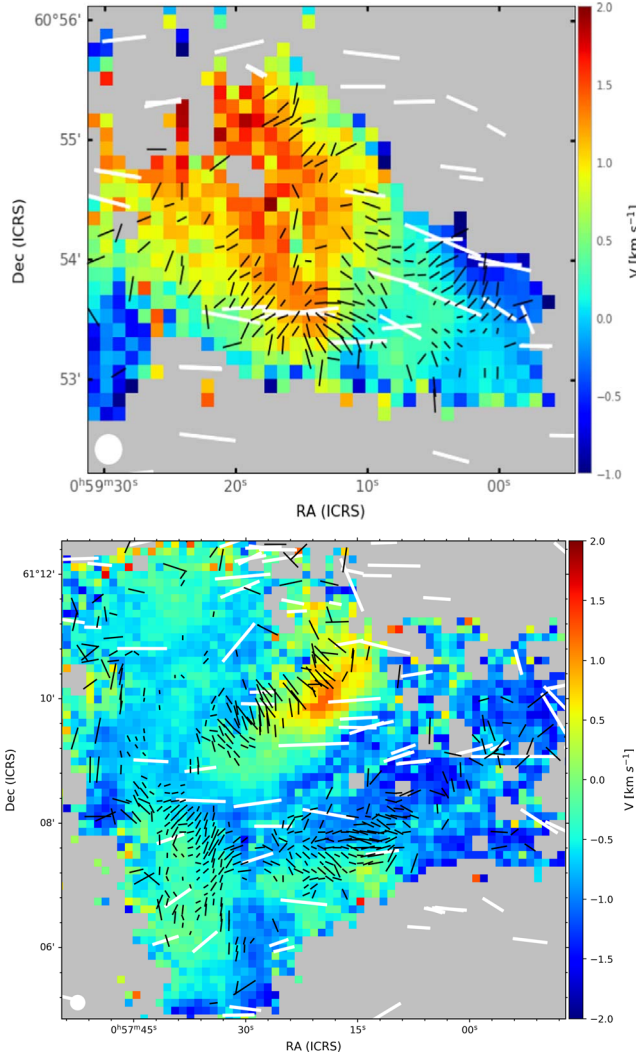
Figure 12. Central velocity maps of IC 63, top, and IC 59, bottom, with their respective velocity gradient vectors plotted in black. Magnetic field polarization vectors are plotted in white on both maps and represent data from Andersson et al. (2013), Soam et al. (2017) for IC 63, and Soam et al. (2017) for IC 59. The length of the lines are representative of the magnitude of the velocity changes for the velocity gradients and the polarization percentages for the magnetic field polarizations in both maps.

contours of the [C II] integrated intensity map of velocities below -0.1 km s^{-1} are plotted in white. These two contours correlate well, with the ionized Hα sitting just outside the cloud of the blueshifted velocities of [C II]. In addition, as shown in Table 1, while the [C II] central velocities range from 0–1 km s^{-1} the HCO$^+$ ($J = 1$–0) velocities only range from $\sim$0.27–0.47 km s^{-1}. This suggests that these two emissions represent the same region
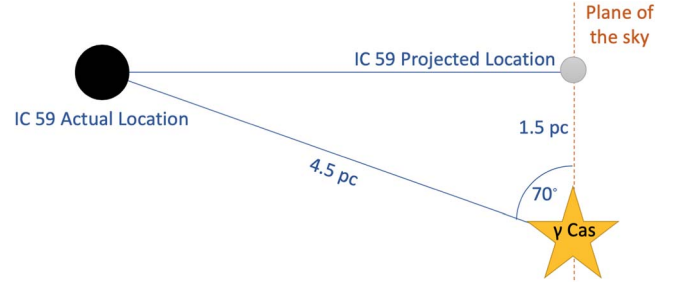

Figure 13. Side view model of the IC 59–γ Cas system with geometrical findings based on G_0 calculations.
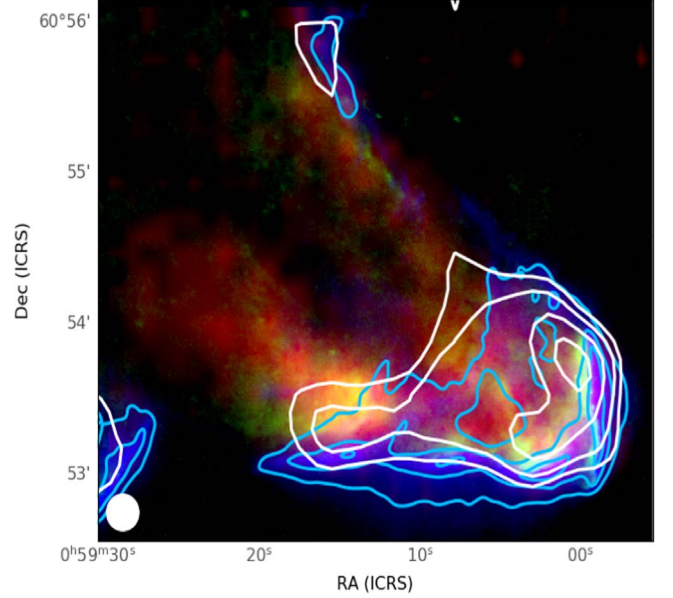

Figure 14. RGB from upper panel of Figure 2 with smoothed contours of [C II] integrated intensity below -0.5 km s^{-1} in white with levels [5, 7, 10, 13] K km s^{-1} and smoothed Hα contours in blue with levels [150, 200, 300] pixel counts. The beam size for the SOFIA [C II] observations, white contour, is plotted in the bottom left-hand corner.

and that the gasses in this region are both being actively ionized and blueshifted, while the rest of the cloud is not. This suggests that IC 63 lies on the far side of γ Cas. Our finding is consistent with findings in Andersson et al. (2013).

Similarly, the RGB images of IC 59 in Figure 3, the channel map in Figure 7, the PV diagrams in Figure 9, and the velocity gradients in Figure 12 show that the Hα emission does not overlap with the dust or gas emissions. Because the Hα emission in IC 59 does not overlap with the rest of the dust or gas emissions, we consider a slightly differently approach than for IC 63. The locations that are closest to the Hα emission are redshifted in IC 59, with $v > 0$ km s^{-1}, which indicates that the emission could be coming from the far side of the cloud. The Hα emission coincident with the [C II] emission would then likely be extincted by the cloud. Figure 15 shows the 250 μm dust map for IC 59 with [C II] integrated intensity contours in white and ^{12}CO (1–0) contours in black. The filled circles and triangles indicate the locations of stars less than 1.25 kpc distance with measures of visual extinctions A$_V$ (Soam et al. 2021d). The yellow circles show stars with an A$_V < 1$ mag, while red triangles indicate stars with an extinction > 1 mag.

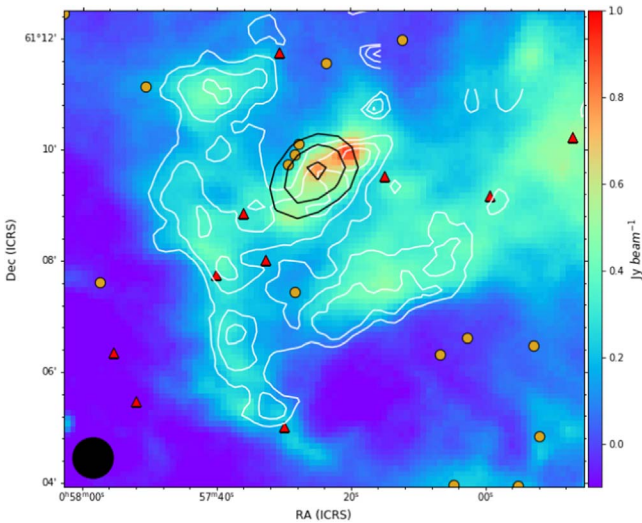The differences in the relative velocities of the high density regions of the two clouds, along with the opposing relative

Figure 15. 250 μm dust map of IC 59 with C [II] integrated intensity contours at levels [10, 13, 16, 20] K km s^{-1} in white for visual reference and ^{12}CO (1–0) contours at levels [1500, 2500, 3300] K km s^{-1} in black. Markers are stars from the VILNIUS Survey within 1250 pc with an A_v less than 1 for the yellow circles and greater than 1 for the red triangles. The beam size of the ^{12}CO (1–0) contours is shown in black in the bottom left-hand corner.
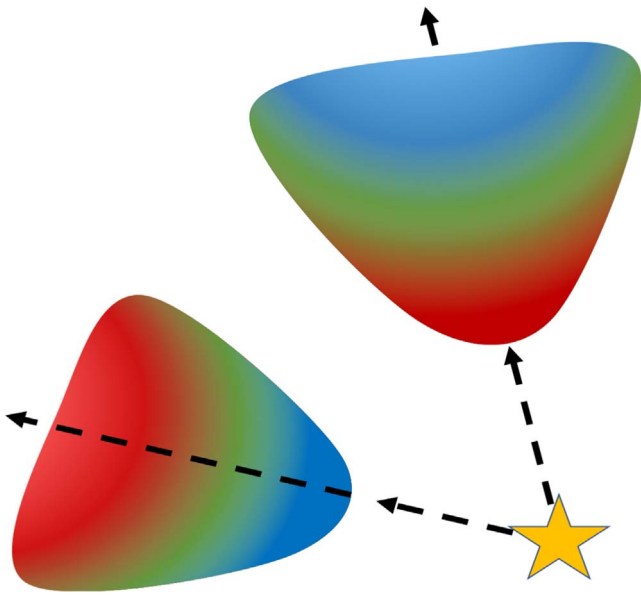

Figure 16. Cartoon model of the γ Cas, IC 59, and IC 63 system. Dashed black lines represent the plane of the sky at the distance of γ Cas.

velocity differences of the diffuse gas emissions in between the arms of each cloud (Section 4.2.2), support the view that IC 59 and IC 63 are on opposite sides of γ Cas. We therefore predict that IC 59 is on the near side of γ Cas.

Our proposed geometric model of the Sh 2-185 system is shown in a simplified form in Figure 16, where the nebulae are modeled by red, green, and blue colors, representing positive, zero, and negative velocities, respectively. The dashed lines from the star indicate the plane of the sky containing γ Cas.

6. Summary

We studied the structure and kinematics of PDRs IC 59 and IC 63 associated with H II region Sh 2-185 using high-resolution SOFIA/upGREAT [C II] observations combined with archival

data on dust emission toward these nebulae. The case of IC 59 and IC 63 presents an interesting example in which the feedback from a B0 star is dominated by photevaporation.

1. The [C II] emission of IC 63 has two clumps with streaming tails showing a velocity shift toward positive velocities, moving away from γ Cas. IC 59 has a less-defined structure, consisting of multiple low density regions and one large core that is redshifted in comparison to the rest of the cloud, which otherwise shift from positive to negative velocities when going away from γ Cas.

2. A G_0 of 115–175 was found for IC 63 using a previously determined inclination angle of 58° (Andersson et al. 2013). Utilizing a G_0 for IC 59 of 25 (Andrews et al. 2018), a distance of 4.5 pc and inclination angle of 70° could be estimated for the cloud.

3. Using [C II] data, we constructed velocity gradients and compared these to plane-of-the-sky magnetic field orientations. We find an anticorrelation between the velocity gradient and magnetic fields in IC 59, but no clear structure in IC 63. The upper limits of our estimations showed that kinetic energy is larger than the magnetic energy in IC 63. This suggests that kinetic pressure in this nebula is dominant.

4. From our analysis of the kinematics and structure of these clouds, we find that IC 63 lies behind γ Cas and IC 59 lies in front.

Appendix
Thermal Pressure

The thermal pressures of these PDRs can be calculated with:

$$\frac{P_{[\text{C II}]}}{k_B} = n_{[\text{C II}]} T_{\text{ex}} \qquad (\text{A1})$$

where n[C II] is estimated from column density assuming that the prominent [C II] region is a cylinder projected as a rectangle, and we assume that the [C II] excitation is thermalized. In IC 63, this cylinder is estimated to have a length of 0.15 pc and radius of 0.05 pc. This gives a one sigma limit of $P_{[\text{C II}]}/k_B$ to be 210.6 K cm^{-3}. If we use $n_{H_2} = 5 \pm 2 \times 10^4$ cm^{-3} (Jansen et al. 1994) and $T_{\text{kin}} = 106 \pm 11$ K (Thi et al. 2009), then we get a P_{H_2}/k_B of 53×10^6 K cm^{-3}. The [C II]/H$_2$ (1–0)S(1) ratio, using our calculated $n_{[\text{C II}]}$ and the n_{H_2} from Jansen et al. (1994), is found to be 1.1×10^{-5}. This is about a factor of 10 off of the abundance ratios that were calculated for the horse head nebula in Bally et al. (2018). This could be partially explained by a difference in volume estimations between our work and Jansen et al. (1994). Using Equation (A1) for [C II] in an area of IC 59 with a length of 0.315 pc and radius of 0.101 pc, the one sigma limit of $P_{[\text{C II}]}/k_B$ is found to be 29.19 K cm^{-3}.

ORCID iDs

Miranda Caputo ⓘ https://orcid.org/0000-0002-2957-3924
Archana Soam ⓘ https://orcid.org/0000-0002-6386-2906
B-G Andersson ⓘ https://orcid.org/0000-0001-6717-0686
Ed Chambers ⓘ https://orcid.org/0000-0003-4195-1032
Rolf Güsten ⓘ https://orcid.org/0000-0002-1708-9289
Lewis B. G. Knee ⓘ https://orcid.org/0000-0002-9342-9003
Jürgen Stutzki ⓘ https://orcid.org/0000-0001-7658-4397

References

Andersson, B. G., Piirola, V., De Buizer, J., et al. 2013, ApJ, 775, 84
Andrews, H., Peeters, E., Tielens, A. G. G. M., & Okada, Y. 2018, A&A, 619, A170
Astropy Collaboration, Robitaille, T. P., Tollerud, E. J., et al. 2013, A&A, 558, A33
Bally, J., Chambers, E., Guzman, V., et al. 2018, AJ, 155, 80
Barentsen, G., Farnhill, H. J., Drew, J. E., et al. 2014, MNRAS, 444, 3230
Code, A. D., & Meade, M. R. 1979, ApJS, 39, 195
Draine, B. T. 1978, ApJS, 36, 595
Drew, J. E., Greimel, R., Irwin, M. J., et al. 2005, MNRAS, 362, 753
Fleming, B., France, K., Lupu, R. E., & McCandliss, S. R. 2010, ApJ, 725, 159
France, K., Andersson, B. G., McCandliss, S. R., & Feldman, P. D. 2005, ApJ, 628, 750
Guan, X., Stutzki, J., Graf, U. U., et al. 2012, A&A, 542, L4
Heyminck, S., Graf, U. U., Güsten, R., et al. 2012, A&A, 542, L1
Hoang, T., Lazarian, A., & Andersson, B. G. 2015, MNRAS, 448, 1178
Hollenbach, D. J., & Tielens, A. G. G. M. 1997, ARA&A, 35, 179
Jansen, D. J., van Dishoeck, E. F., & Black, J. H. 1994, A&A, 282, 605
Jansen, D. J., van Dishoeck, E. F., Black, J. H., Spaans, M., & Sosin, C. 1995, A&A, 302, 223
Jansen, D. J., van Dishoeck, E. F., Keene, J., Boreiko, R. T., & Betz, A. L. 1996a, A&A, 309, 899
Jansen, D. J., van Dishoeck, E. F., Keene, J., Boreiko, R. T., & Betz, A. L. 1996b, A&A, 315, 327
Karr, J. L., Noriega-Crespo, A., & Martin, P. G. 2005, AJ, 129, 954
Lancaster, L., Ostriker, E. C., Kim, J.-G., & Kim, C.-G. 2021, ApJL, 922, L3
Lazarian, A., & Hoang, T. 2007, MNRAS, 378, 910
Miao, J., Sugitani, K., White, G. J., & Nelson, R. P. 2010, ApJ, 717, 658
Miao, J., White, G. J., Thompson, M. A., & Nelson, R. P. 2009, ApJ, 692, 382
Osterbrock, D. E. 1957, ApJ, 125, 622
Pabst, C. H. M., Goicoechea, J. R., Teyssier, D., et al. 2020, A&A, 639, A2
Pety, J. 2005, in SF2A-2005: Semaine de l'Astrophysique Francaise, ed. F. Casoli et al., 721
Polehampton, E. T., Wyrowski, F., & Schilke, P. 2005, in IAU Symp. 231, Astrochemistry: Recent Successes and Current Challenges, ed. D. C. Lis, G. A. Blake, & E. Herbst, 148
Risacher, C., Güsten, R., Stutzki, J., et al. 2016, A&A, 595, A34
Soam, A., Andersson, B. G., Acosta-Pulido, J., et al. 2021a, ApJ, 907, 93
Soam, A., Andersson, B. G., & Acosta-Pulido, J. 2021b, ApJ, 907, 93
Soam, A., Andersson, B. G., Karoly, J., DeWitt, C., & Richter, M. 2021c, ApJ, 923, 107
Soam, A., Andersson, B. G., Straižys, V., et al. 2021d, AJ, 161, 149
Soam, A., Maheswar, G., Lee, C. W., Neha, S., & Andersson, B. G. 2017, MNRAS, 465, 559
Thi, W. F., van Dishoeck, E. F., Bell, T., Viti, S., & Black, J. 2009, MNRAS, 400, 622
Wolfire, M. G., Vallini, L., & Chevance, M. 2022, ARA&A, 60, 247
Young, E. T., Becklin, E. E., Marcum, P. M., et al. 2012, ApJL, 749, L17